Materials & Design 231 (2023) 112058

Contents lists available at ScienceDirect

Materials & Design

journal homepage: www.elsevier.com/locate/matdes

Fracture toughness of wood and transparent wood biocomposites in the toughest LT-direction

Erik Jungstedt [a], Marcus Vinícius Tavares Da Costa [c], Sören Östlund [b], Lars A. Berglund [a,*]

[a] KTH Royal Institute of Technology, Department of Fiber and Polymer Technology, Wallenberg Wood Science Center, SE-100 44 Stockholm, Sweden
[b] KTH Royal Institute of Technology, Department of Engineering Mechanics, SE-100 44 Stockholm, Sweden
[c] Karlstad University, Department of Engineering and Chemical Sciences, Karlstad, Sweden

HIGHLIGHTS

- Delignified birch/poly(methyl methacrylate) biocomposites show higher fracture toughness across the fiber direction than native birch.
- Fracture toughness of polymer-filled delignified birch composites is improved due to increased peak cohesive stress in the damage zone.
- Fiber bundle bridging and pull-out are the observed fracture mechanisms of transparent birch/poly(methyl methacrylate) from microscopy.

GRAPHICAL ABSTRACT

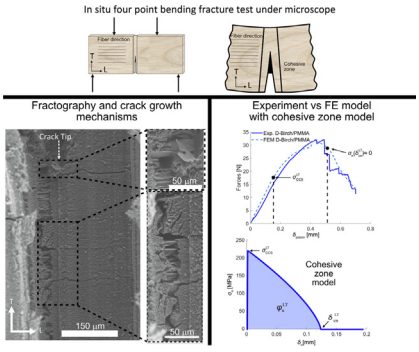

ARTICLE INFO

Article history:
Received 14 April 2023
Revised 22 May 2023
Accepted 31 May 2023
Available online 5 June 2023

Keywords:
In situ fracture test
Orthotropic
Cohesive zone
Microscopy
Multifunctional materials

ABSTRACT

Fracture toughness and mechanisms of crack growth are characterized for transparent wood polymer biocomposites and compared to native wood, with the crack normal to the fiber direction (LT fracture plane). Side-grooved specimen geometries generated pure mode I crack growth, whereas previous investigations commonly report 90° crack path deflection. Crack growth micromechanisms were analyzed by experimental fracture tests and in-situ microscopy observations. Large damage zones around the crack tip with fiber bundle bridging and pull-out were observed in the crack wake, justifying more advanced cohesive zone modeling suitable for composite materials design. The polymer matrix resulted in much higher fracture energy of the biocomposites compared to native wood due to increased local cohesive strength. This strength increased from the polymer contribution and more homogeneous stress distribution in the wood fibers.

1. Introduction

Transparent wood biocomposites (TW) are wood substrates where the pore space is filled with a polymer matrix phase [1]. They combine excellent mechanical properties with high optical transmittance and may be more sustainable alternatives to fossil-based plastics with optical transparency (polystyrene, poly(methyl methacrylate), polycarbonate) [2], with better mechanical performance. However, there are few transparent materials available. TW composites could, for instance, serve in lighting applications where the light-emitting diode function is integrated into the composite using quantum dots [3], while the TW panel is semi-structural with a load-bearing function. Optically transparent biocomposites are multifunctional engineering materials with the po-

* Corresponding author.
E-mail addresses: erikjun@kth.se (E. Jungstedt), marcus.tavares@kau.se (M.V.T. Da Costa), soren@kth.se (S. Östlund), blund@kth.se (L.A. Berglund).

https://doi.org/10.1016/j.matdes.2023.112058
0264-1275/

tential of being fully bio-based [4], and may, for example, be used as translucent windows, thermal batteries [5], and translucent plywood laminates for interior design [6].

The LT fracture toughness in the toughest direction is not well understood for TW composites or other wood-polymer composites with polymer filling the wood pore space. Wood itself is considered a tough material in general material comparisons and this is certainly true when related to density. Ashby and Gibson [4] show that LT fracture toughness scales with volume fraction of solid content in wood [7]. Typical values for LT critical strain energy release rate (G_c) of wood species used in building applications are ≈ 10 kJ/m^2. As a comparison, Bernstein [8] reported J_c values for polycarbonate for unstable crack growth of ≈ 7 kJ/m^2.

A problem with previous work on LT fracture toughness of wood is that even though the initial crack is oriented normal to grain (fiber direction), the crack path rapidly deviates and runs parallel to grain; this is apparent if early work is read carefully [9–13]. This is addressed here. Another limitation is that despite the complexity of crack growth mechanisms [9–11] and presumably large damage zones (DZ), all studies mentioned are based on linear elastic fracture mechanics (LEFM), where the extension of the DZ in the crack wake of a moving crack tip is assumed to be small compared with, e.g., the crack length. Thus, fracture toughness is simply estimated from the peak load and LEFM [12]. LT fracture toughness (-critical stress intensity factor, K_c, or G_c) for wood show typical G_c data in the range 6–18 kJ/m^2 [9,14,15]. From previous wood-polymer composites literature, we could only find wood composite toughness data from impact bending tests [16], which are not true material properties.

The fracture toughness of the weaker fracture planes in wood, where the crack path runs parallel to the fiber direction, is less than one tenth of the LT fracture toughness [7]. The lower fracture toughness is related to the lower local strength for cell wall peeling and fiber cross-over bridging mechanisms, which are less fracture resistant than pull-out and fiber breakage mechanisms [17]. For this reason, crack growth in the weak RL and TL fracture planes is common during failure of native wood and TW composites [18]. The fracture toughness of wood is anisotropic also in a more general sense, and at least eight crack paths have been defined [12]. For timber structure modeling, or wood composites, where growth ring structures are common, it is often important to include several fracture planes in the analysis [19,20]. The tough LT fracture plane is often neglected as it is assumed that the crack only grow towards the weaker fracture planes [20]. Few studies focus on LT fracture toughness which also limits the understanding of the fracture mechanisms, which are particularly interesting for design of new composites.

Here, fracture toughness properties are estimated using an approach suitable for LT wood composite toughness using cohesive zone modeling (CZM) and experiments on single-edge precracked four-point bending (4 PB) specimens. Microscopy reveals fracture mechanisms in the DZ, and observations are helpful in verifying and interpret CZM parameters. All damage and sources of non-linearity are assumed to be located within the cohesive zone; the surrounding bulk material is an orthotropic linear elastic composite. CZM parameters are the fracture properties of the cohesive zone that represents the DZ: cohesive fracture energy, critical strength, and limiting separation. These CZM parameters facilitate analysis of crack growth micromechanisms; the CZM approach also gives more information for materials design purposes than point criteria (K_c, G_c). Previously studied TW composites are used [18,21], where native wood (birch) is compared with two polymer-filled biocomposites: native birch impregnated with poly(methyl methacrylate) (Birch/PMMA), and optically transparent delignified birch impregnated with PMMA (D-Birch/PMMA).

The main objective is to enforce LT crack growth in side-grooved fracture mechanics specimens to estimate mode I fracture properties for three orthotropic wood materials and to clarify local fracture micromechanisms for the purpose of materials development. In-situ fracture tests and real-time recording of microscopy images are used to interpret crack growth mechanisms and compare crack growth in porous native wood and polymer-filled wood biocomposites. Data are not validated for engineering design purposes; it is still challenging to manufacture sufficiently large and thick specimens of transparent wood biocomposites. A fitted model using the finite element method (FEM), including DZ description in the LT fracture plane using CZM, helps validate experimentally determined LT fracture toughness parameters and improve accuracy.

2. Materials and methods

2.1. Materials

Crown-cut silver birch veneers (*Betula Pendula)*, free from knots, were bought from Holm Trävaror AB (Sweden), with an oven-dried density of around 590 kg/m^3, measured after one week of conditioning in an oven at 105° C. The moisture content was determined to be about 8 %, calculated by the relative difference of the sample weight before (conditioned in 50 % relative humidity) and after oven-drying. The thickness of the veneers was around 2.5 mm, measured with a digital dial indicator (Mitutoyo S112SB, Japan). The same type of veneer sheet was used to produce transparent wood biocomposites. The veneers were specifically cut so that the samples had the tangential (T) and longitudinal (L) wood microstructural directions in-plane and radial (R) direction out-of-plane to ensure that the wood microstructural directions coincided with the orthotropic material directions L, T and R. In native wood, six fracture planes are commonly postulated to describe the crack growth paths [22], denoted by two indices of the three material directions L, T, and R; the first index denotes direction normal to the fracture plane and the second index denotes the crack propagation direction, (see Fig. 1a). The specimens were cut to ensure a machined crack was oriented along the LT fracture plane.

2.2. Material preparation

Three materials were investigated: native birch, birch impregnated with PMMA (Birch/PMMA), and delignified birch impregnated with PMMA (D-Birch/PMMA). Delignification is carried out to remove chromophores and allow high optical transmittance [23]. The neat polymer matrix PMMA was included for comparing fracture properties.

The biocomposite processing is explained in previous work [21]. First, chemical delignification of birch veneer is carried out to remove lignin and its chromophores. The veneers were soaked in water, which later was replaced with acetone to assist monomer (methyl methacrylate) impregnation. The monomer was polymerized to PMMA in an oven in situ with the delignified birch template to produce D-Birch/PMMA. The same biocomposites process was used to produce Birch/PMMA, without the delignification-step. The thickness of the final biocomposites was $h \approx 2.8$ mm with no visually observable defects, and the thickness of native birch veneers was $h \approx 2.5$ mm.

3. Experimental setup and specimen preparation

A four-point bending (4 PB) setup was used to measure the fracture toughness of small wood-based biocomposites see Fig. 1, with

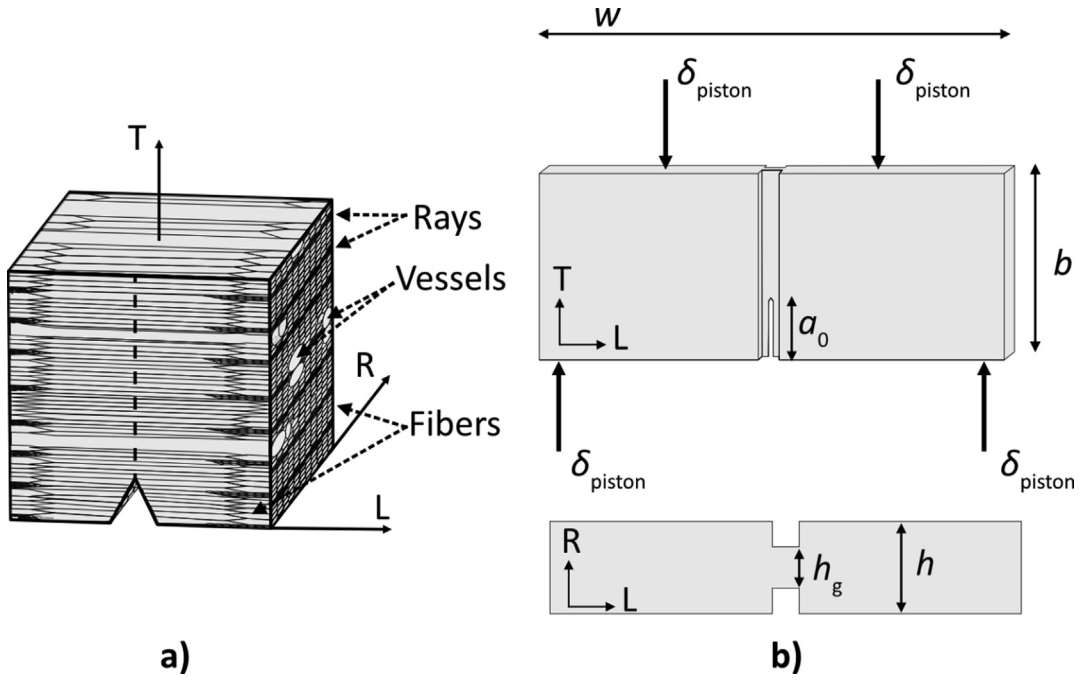

Fig. 1. Illustration of LT crack orientation in wood with material axes coinciding with three orthogonal directions: longitudinal (L), radial (R), and transverse (T) direction. The dashed black line shows the crack growth direction. b) 4 PB side-groove specimen geometry, including material directions. δ_{piston} is the applied displacement on the 4 PB supports, w is the width of the sample, h is the thickness, h_g is the side-groove thickness, b is the height, and a_0 is the initial crack length.

steel rollers at support and load points. The 4 PB was performed in displacement control with prescribed displacement, δ_{piston}, on the roller supports. The specimens were prepared with side-grooves to promote crack growth of LT-oriented pre-crack, as has been done for ceramic composites [24] and glass fiber-reinforced polymer composites (GFRP) [25]. Three to five samples were tested for each specimen configuration.

The 4 PB fracture tests were done in situ in a microstage (Deben MT200, UK) under optical microscope (OM, Leica GmbH, M205 FA, Germany) and inside a scanning electron microscope (SEM, Hitachi TM-1000, Japan). Videos of OM images from in situ fracture tests are provided as supplementary videos (Birch.avi, Birch_PMMA.avi, and D-Birch_PMMA.avi). A 200 N load cell was used, and displacement speed was 0.1 mm/s. Steel cylinder supports had a diameter of 5 mm, a fixed load span of 5.5 mm, and a support span of 23.5 mm. The microstage limited specimen dimensions, and the side-groove specimens were lasered to w = 30 mm, and b = 3 mm. The initial crack length was $a_0 \approx 1.1$ mm with a sharp pre-crack made using a 100 μm thick razor blade.

The side-grooves were cut on each side with a remaining thickness of $h_g \approx 1$ mm. The side-grooves were widened with a 0.4 mm thin jigsaw blade. A high-resolution field-emission SEM (FE-SEM, Hitachi, S-4800, Japan) was also used with the same experimental setup. For SEM and FE-SEM, specimens were prepared with a conductive coating of palladium (Pd) for 20 s with a sputter coater (RMC PowerTome MT-XL, UK).

3.1. Fracture properties

In previous work [18], strain field measurements showed that the fracture process zone of TL crack growth could be modeled with a cohesive zone model (CZM), but LT fracture toughness and crack growth micromechanisms for the wood-polymer biocomposites are unknown. Since fiber composites can be described by cohesive zone equivalent models [17] due to fiber bridging mechanisms, our hypothesis is that the CZM approach will be applicable. We start by estimating experimental fracture toughness based on the J-integral [26] and maximum force as a crack initiation criterion. Start values for CZM parameters for the three materials were estimated from these experiments. In the next step, experimental load–displacement results were analyzed using finite element analysis (FEA) of orthotropic composites combined with the CZM describing damage development at the crack region. The CZM parameters were fitted to experimental data, and final CZM fracture properties were obtained for the neat birch, Birch/PMMA, and D-Birch/PMMA. All non-linear effects are assumed to result from the cohesive zone (DZ).

The path-independent J-integral for a bending load case was first used to estimate the LT fracture energy at crack growth from the 4 PB fracture tests of the side-grooved specimens [26],

$$J = \frac{2}{h_g}\frac{U(F_{max})}{b - a_k}, k = (0, 1, 2, ...) \quad (1)$$

where $U(F_{max})$ is the total potential energy at peak load F_{max} measured by integration of the load–displacement curve up to F_{max}, and a_k is the crack length where k indices correspond to increased crack extension and a_0 is the initial crack length. The original crack length, a_0, and the momentaneous crack length, a_k, were measured from recorded videos with OM and SEM in the in-situ 4 PB fracture test.

3.2. FEM modeling using the cohesive zone model

Fig. 2 illustrates the model to describe the mechanical behavior of the present materials. The dashed line symbolizes the LT fracture plane where cohesive zones in the FEM are located and where all damage is developed behind the crack tip; the rest of the material is orthotropic linear elastic in nature. First, start values for CZM fracture energy are estimated from J_c and cohesive critical strength, σ_{ccs}, which is based on previously determined tensile strength [21]. Then FE-model with initial CZM parameters are compared with load–displacement of the 4 PB fracture mechanics specimens.

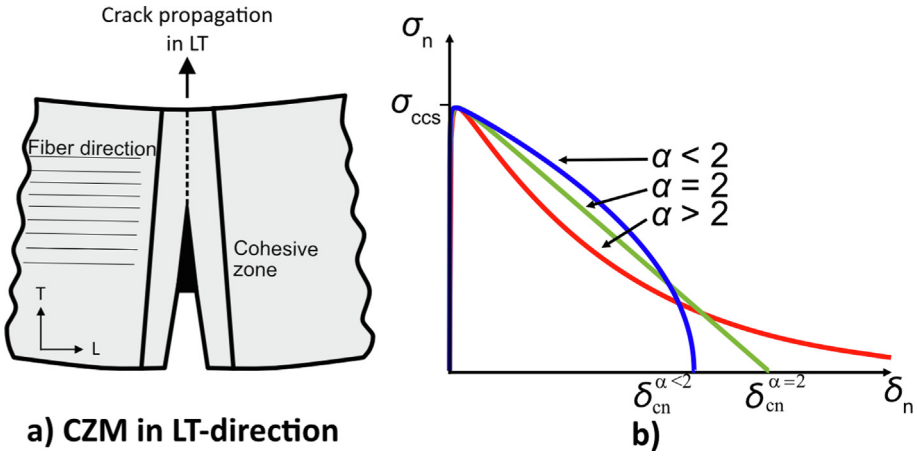

Fig. 2. a) Model of the side-grooved specimen, designed as in Fig. 1b, in FEM with a cohesive zone along the LT fracture plane (dashed line). b) A plot showing the relation between cohesive stress in normal direction, σ_n, and separation,δ_n, with different cohesive softening shapes, controlled by α, of the PPR model. Here, σ_{ccs} is the cohesive strength, δ_{cn} is the limiting separation (dependent on α), and φ_n the cohesive fracture energy corresponding to the area under the curve.

The CZM parameters are further adjusted for improved fit to give the final CZM fracture properties. Fig. 2b) is the cohesive stress-separation relation of the CZM. The CZM parameters to be determined represent the fracture properties of the present materials [17]. For validated CZM fracture properties, they can be used to predict notched strength of any structural geometry also under large-scale damage conditions. The cohesive stress can be expressed as

$$\sigma_n = \sigma_{ccs}\chi(\delta_n/\delta_{cn}), \tag{2}$$

where "n" denotes the normal direction from the fracture surface, χ is a dimensionless function that describes the shape of the relation, σ_{ccs} is the critical cohesive strength at which damage is initiated, δ_n is separation distance, and δ_{cn} is the limiting separation at which the cohesive stress is zero and the bridging ligament fails. The cohesive fracture energy represents the area under the cohesive stress-separation relation and is

$$\varphi_n = \int_0^{\delta_{cn}} \sigma_n \, d\delta_n, \tag{3}$$

where complete failure of the cohesive zone occurs at δ_{cn}.

The CZM describes the fracture behavior of an element in the DZ and is based on non-linear softening. The crack propagation path was known from experimental observations. The crack propagation path follows the LT fracture plane assuming only mode I opening fracture since the 4 PB load case was symmetric, see Fig. 1b.

The cohesive softening relation was based on a potential-based CZM developed by Park et al. (PPR) [27], available for implementation into Abaqus through a user-element subroutine [28]. Details of the PPR cohesive model are found in [27]. A brief overview of the cohesive stress-displacement relation is included in Appendix C. PPR is essentially formulated as a mixed-mode CZM, used to evaluate mode I LT cohesive fracture. The damage process of the cohesive zone is initiated when $\sigma_n = \sigma_{ccs}$, and the shape of the subsequent softening relation is controlled by a shape parameter, α, see Fig. 2b. Complete separation of the fracture surfaces of the cohesive zone occurs when $\delta_n = \delta_{cn}$ is reached (e.g.,$\sigma_n = 0$, see Fig. 1b). Eq. (2) provides a fracture criterion with σ_{ccs} and δ_{cn} as important parameters. The fracture energy of the cohesive relation, φ_n, is the area under the stress-separation curve in Fig. 2b, see also Eq. (3).

The in-plane properties of the materials were assumed to be orthotropic linear elastic with four elastic parameters: E_L, E_T, ν_{LT}, G_{LT}, and under plane stress. The orthotropic linear elastic properties were known from previous tensile tests [21], and G_{LT} for Birch/PMMA was assumed to be the same as for D-Birch/PMMA.

The FEM analysis was processed with an implicit solver in batch mode on a desktop computer with a six-core processor (Intel Xeon E5-1650 v3, 3.5 GHz), 16 GB RAM, and NVIDIA Quadro M2000 (4 GB RAM) in the FEM software Abaqus. A quad mesh was generated in Abaqus with elements concentrated along the crack paths and a cohesive element side length of about 0.025 mm. Four-noded elements with reduced integration (CPS4R) and hourglass control were used to analyze elements with only linear elastic bulk properties. The PPR cohesive zone user elements were attached between the CPS4R elements at the intended and assumed crack paths. The element thickness was set to the corresponding sample thickness. Boundary conditions mimicked the 4 PB experimental setup with four rigid cylinder supports. The bottom supports are fixed and the upper supports displaced with prescribed displacement. Contact formulation is frictionless between the specimen and the 4 PB support cylinders.

4. Results and discussion

4.1. Fracture toughness

In the first stage we determine J_c. Table 1 presents fracture toughness data for mode I opening fracture determined from load-displacement curves of side-grooved specimens, see Fig. 1b. The grooved specimen geometry may force the crack to move in the prescribed direction [25], which was indeed successful. In contrast to previous wood fracture investigations, we may analyze LT crack growth rather than just conditions for crack initiation. Non-linear behavior was apparent from the load–displacement curve, Fig. 3a, and LT crack growth in direction of the original crack commenced at peak load, F_{max}. At crack growth initiation, J_c was determined from Eq. (1) using the initial crack length a_0 and the entire load–displacement curve until F_{max} (see Fig. A1 in Appendix); results are found in Table 1. Birch/PMMA and D-Birch/PMMA show

Table 1
Fracture properties with J_c determined at crack growth initiation; σ_{ccs}^{LT} is based on previous tensile strength data [21].

Materials	J_c [kJ/m^2]	σ_{ccs}^{LT}[MPa]
Birch	8.1 ± 2.6	170[1]
Birch/PMMA	13.5 ± 3.6	220[1]
D-Birch/PMMA	14.8 ± 3.7	270[1]
PMMA	1.1	

[1] Tensile strength data from previous work [21].

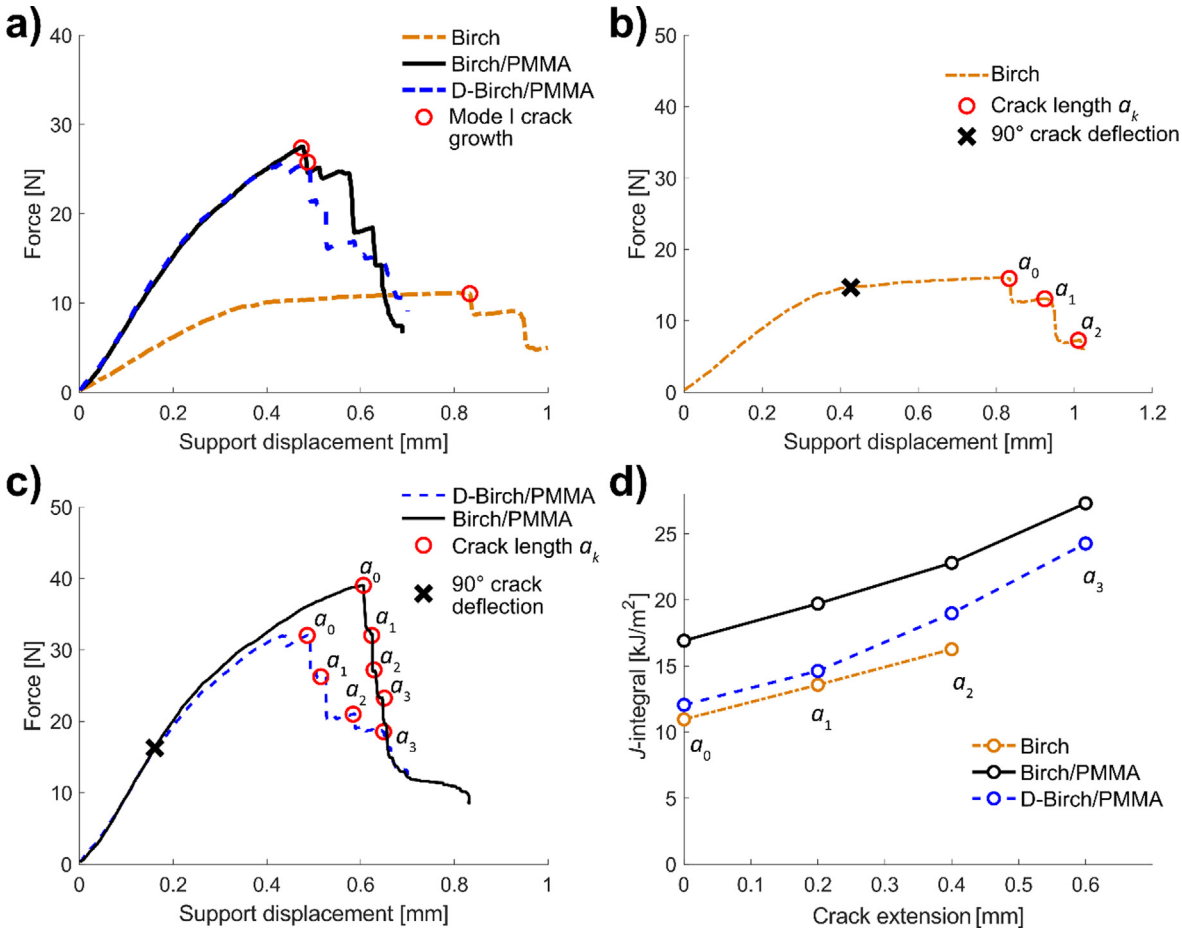

Fig. 3. Typical load–displacement curves for side-grooved LT specimens of Birch, Birch/PMMA, D-Birch/PMMA; a) Side-grooved specimens with mode I crack growth initiation indicated with a red circle; b) Birch; c) Birch/PMMA and D-Birch/PMMA. The crack length, a_k, has indices k, each corresponding to increased crack length of 200 μm; d) J-integral values as a function of crack length a_k for the three individual specimens in b) and c). Note that J_c for the Birch specimen in 3d) is higher than the average value in Table I. (For interpretation of the references to colour in this figure legend, the reader is referred to the web version of this article.)

larger J_c values than Birch, and the non-linear behavior is more pronounced for Birch. Micro-scale damage development along the fiber direction at the crack tip was observed by OM, within the confined groove region, marked with "**x**" in Fig. 3b-c.

The post-peak behavior of the specimens (Fig. 3a-c) show a "staircase"-like behavior. This has been observed for balsa-epoxy biocomposites (4 PB tests), although low-density balsa (low wood volume fraction) resulted in low fracture energy, $G_c \approx 2.5$ kJ/m^2 [29], compared to Table 1. In the present study, crack growth extensions, each of about 200 μm, were observed and explain the "staircase" softening behavior, indicated by red circles in Fig. 3b-c. In Fig. 3d, Eq (1) is evaluated at each new crack length (e.g., $a_1 \approx a_0 + 200$ μm), shown in Fig. 3b-c, and J increases with crack length as the DZ size is increased. In the FEA section we will estimate fracture mechanics properties using a CZM, and data from Table 1 will be used as start values for the fitting approach. The start value for CZM fracture energy in the LT direction, φ_n^{LT}, is obtained from $\varphi_n^{LT} = J_C$ and corresponding critical cohesive strength, σ_{ccs}^{LT}, start values are assumed to be the measured tensile strengths [21]; see Table 1.

4.2. Micromechanisms of crack growth

Figs. 4–5 are sequential images of the fracture process zone in Birch and D-Birch/PMMA side-grooved specimens from in-situ 4 PB fracture tests in table-top SEM and FE-SEM. Crack growth occurs at peak load, and prior damage mechanisms in the fracture process zone are dominated by multiple sub-critical microcracks in the weakest TL fracture plane; see Fig. 4. At LT crack growth initiation, the crack rapidly extended about 200 μm, impeded by crack growth in the TL direction. Additional images are presented in Fig. A2 in Appendix B. For D-Birch/PMMA in Fig. 4a, fractured PMMA rods are present in the large vessel channels; a bridging bundle of fibers is also observable, and crack growth by 90° deflection is observed (along the fiber direction). The D-Birch/PMMA crack growth micromechanisms are influenced by local wood reinforcement microstructure. The same was observed for Birch/PMMA; see Fig. A3. Ray cells perpendicular to the fiber direction are found adjacent to cracks growing and deflecting in the 90° TL direction. This agrees with cracking in unnotched impact specimens of related sugar maple biocomposites with polymer matrix [30]. For native Birch, the fracture observations appear similar to Birch/PMMA biocomposites, except that wood fibers seem torn, exposing their cell lumen interior.

Fig. 5 shows corresponding higher resolution in-situ images of D-Birch/PMMA in FE-SEM. Details of microcrack formation, fiber bridging, 90° crack deflection following ray cell regions, and fractured vessels filled with PMMA are apparent. Subsequent images with increasing load can be seen in Fig. A4. We conclude that fiber bundle bridged microcracks were formed in the LT fracture plane, ahead of the LT crack tip, followed by sudden crack deflection in

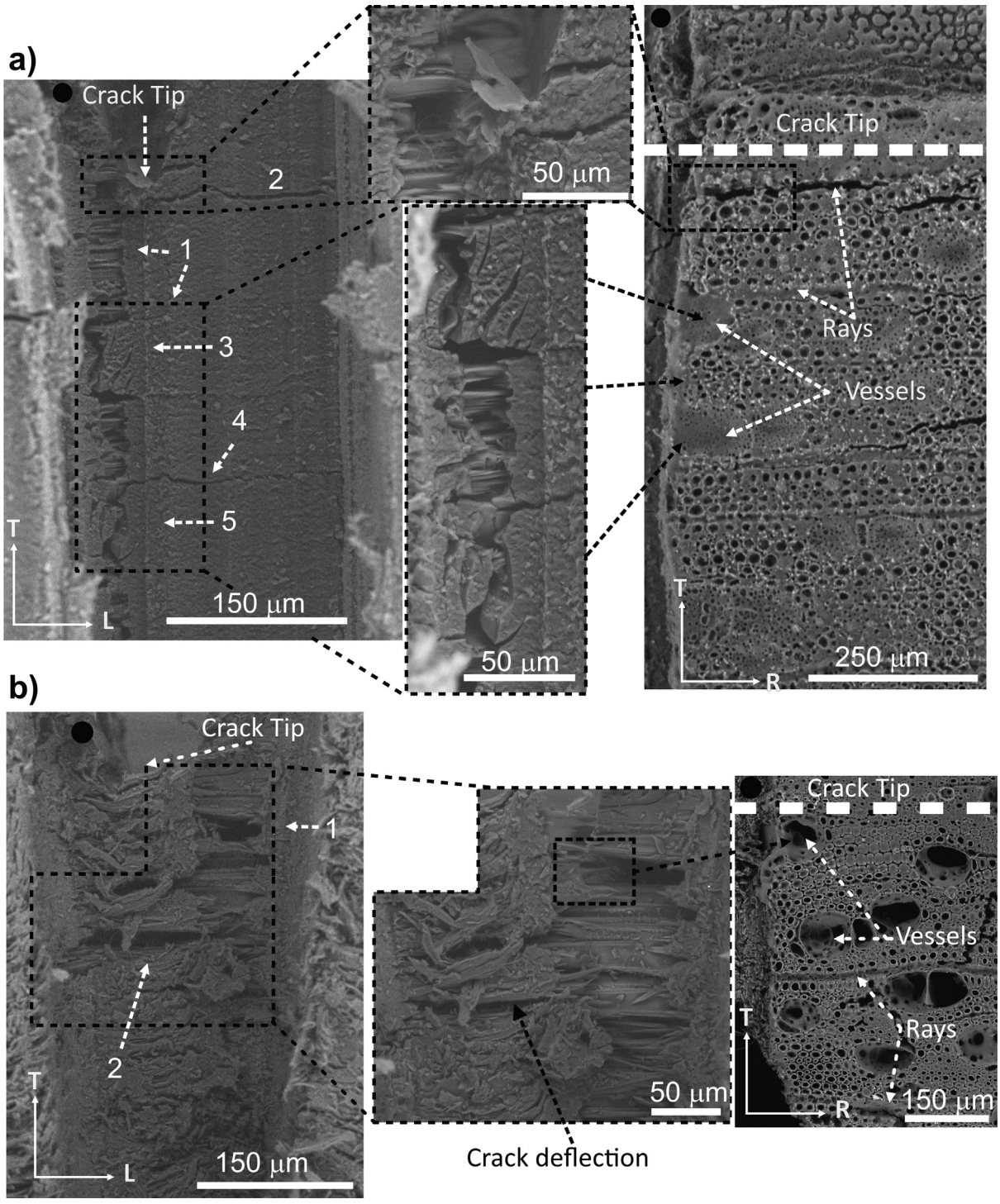

Fig. 4. Side-view fractography of a) D-Birch/PMMA and b) Birch side-grooved specimens with numbered sequences (e.g., 1,2…5) indicating the order of the fracture event observed by in-situ 4 PB tests in SEM. For subsequent images see Fig. A2 in Appendix B. Middle column shows magnified regions. Note coordinates in right images in a) and b) which are laser cut cross-sections, cut in T-R plane along the crack path in T-direction.

the direction parallel to the fibers. Fiber cell bundles are bridging the crack, a representative characteristic of the DZ. Magnified images reveal damaged ray cells at the crack tip, influencing the 90° crack deflection. In all microscopic images, 90° crack deflection is impeded at the side-groove edges, see Fig. 5. The present LT failure mechanisms are very different compared with TL fracture tests (weak direction) of D-Birch/PMMA, where comparably flat, brittle fracture surfaces with crossing ray cells are observed [14]. TL fracture energies were low, explained by cell wall peeling mechanisms.

The higher resolution FE-SEM images in Fig. 5 show fiber bridging zones and fractured PMMA rods in vessel regions, similar to Fig. 4a. At high magnification, fiber bundle fractures are apparent, and PMMA in the cell lumen is exposed, suggesting weak PMMA-cell wall interfacial adhesion [1]. For brittle fiber-reinforced ceramic composites loaded parallel to the fiber direction, the crack often jumps between fiber–matrix interfaces [31]. For the present biocomposites, crack growth through the cell wall combines with fiber bundle bridging and pull-out. Fiber bundle pull-out is expect-

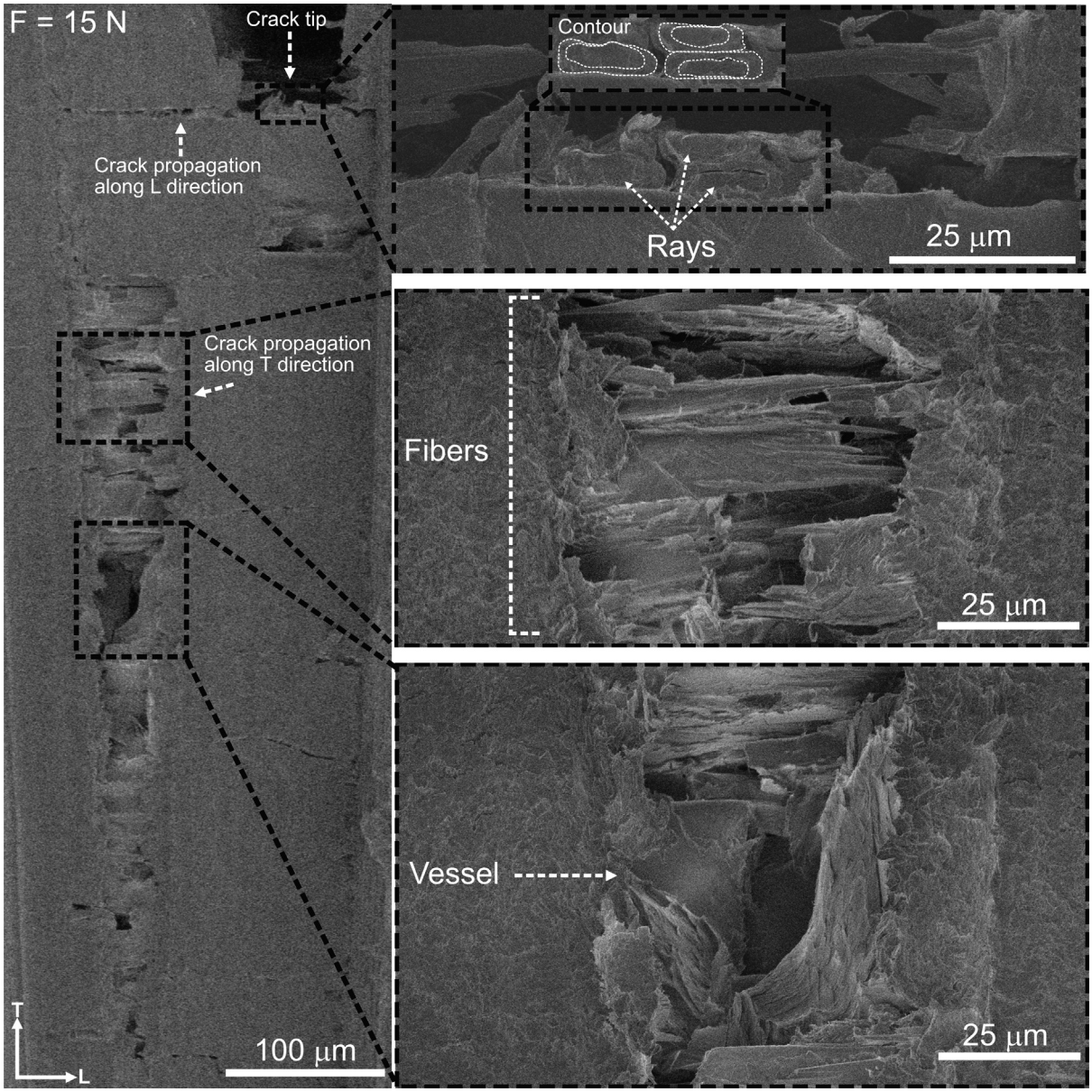

Fig. 5. Side-view FE-SEM fractography of fiber bridged D-Birch/PMMA after peak-load. The left image shows an overview of the LT crack state with three regions enclosed by black-dashed boxes, with magnified images in the right column. The upper right image shows three cleaved ray cells oriented in the R-direction (out-of-plane of the image) located at the crack tip.

ed to absorb significant energy [32] and Fig. 5 suggests significant fiber pull-out contributions to the toughness. This is in contrast with conclusions from early work on LT toughness of wood [9,10], where 90° crack deflection and lack of LT crack growth observations hampered interpretation of mechanisms.

4.3. Analysis of the CZM_{LT} properties for LT crack growth

In this section, FEM is combined with a CZM approach to estimate CZM parameters. The CZM model approach is more versatile than LEFM since CZM properties can be linked to microstructure and also to analysis of cases with large DZs compared with crack lengths and other structural dimensions [17].

Fig. 6a presents the results from the FE-model with the side-grooved specimen geometry of the D-Birch/PMMA specimen compared to experimental data. CZM parameters in the LT direction (CZM_{LT}) obtained from Table 1, and matching functional shape of the stress-separation relation is evaluated by different values on α (see Fig. 2b). The initial CZM_{LT} limiting separation δ_{cn}^{LT} is obtained from values in Table 1 for σ_{ccs}^{LT} and $\varphi_n^{LT} = J_c$ combined with Eq. (3), and shape parameter α, see details of the potential-based PPR model in Appendix C. The FE-model is slightly stiffer than experimental data for Birch/PMMA and D-Birch/PMMA, possibly due to variations in sample stiffness since the average elastic properties from previous tensile tests [21] are used in the model. Different cohesive softening shapes (controlled by α) influence the length of the fracture process zone and the non-linear global behavior in the load–displacement relation for the specimen. From Fig. 6a, a value of α between 1.5 and 2.0 have the closest match between FEM and experimental data compared to the more brittle cohesive softening relation (α = 5.0), which underestimates the peak load. Subcritical damage and fiber bundle pull-out mechanisms are ob-

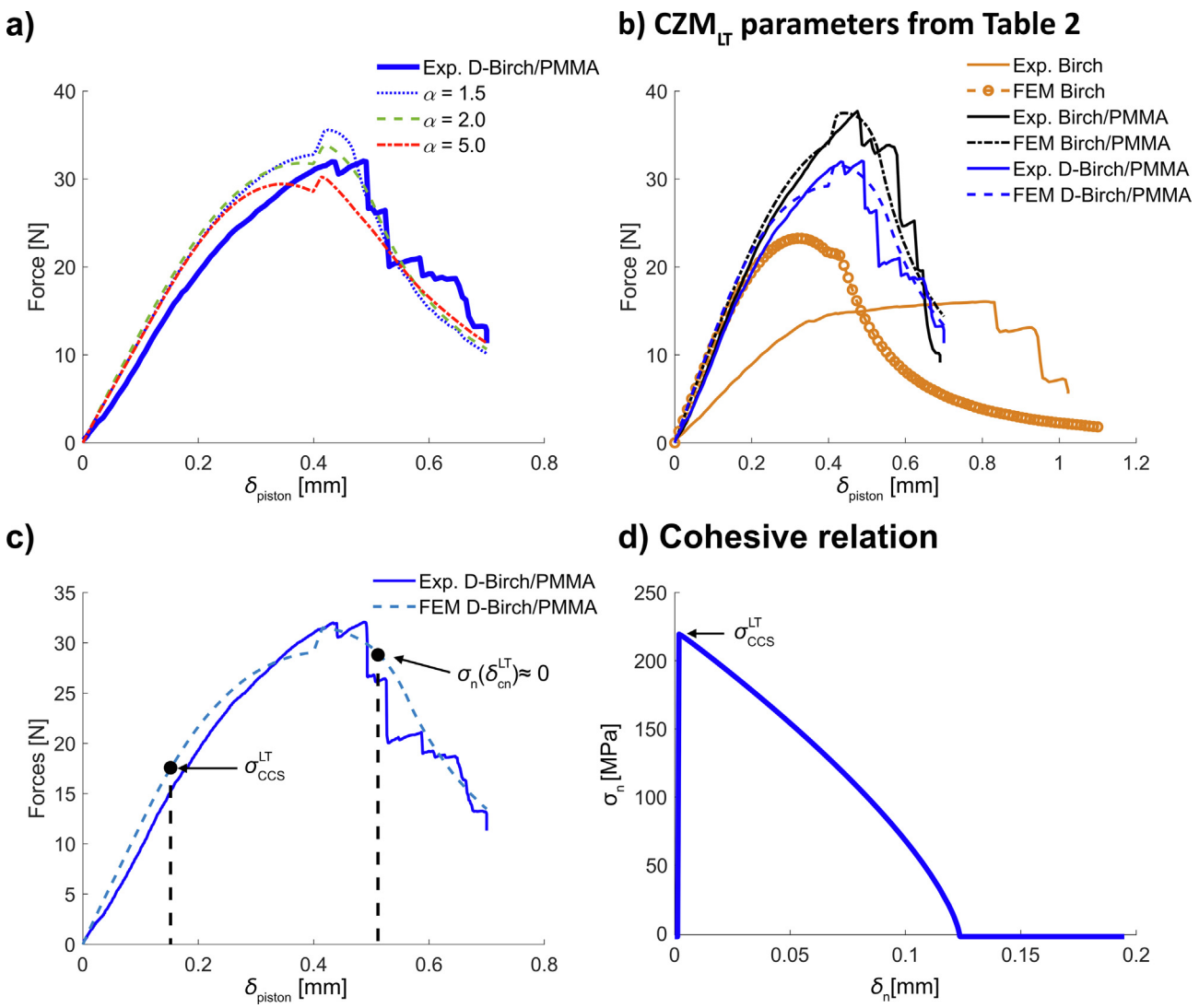

Fig. 6. Experimental and FEM load–displacement curves of side-grooved specimens. a) FEM load–displacement data with different values of the softening shape parameter α are compared with experiments for a D-Birch/PMMA specimen. Values on and are imported from Table 1. b) Birch, Birch/PMMA, and D-Birch/PMMA experiment and FEM results with calibrated CZM_{LT} parameters. c) Experimental data of D-Birch/PMMA with arrows showing where in the load–displacement curve of the FEM model the cohesive zone is developed, and at $\sigma_n = 0$ crack growth is initiated. c) Cohesive softening relation for D-Birch/PMMA using the CZM_{LT} parameters from Table 2.

served in the micrographs in Figs. 4-5 before F_{max} in the load–displacement curves in Fig. 6a. This is modeled as stiffness degradation in the specimen by damage development described by the CZM_{LT} softening behavior. Crack growth occurs around F_{max}, without catastrophic loss in load-bearing capacity of the specimen. From the in situ observations, the DZ extension is large compared with initial crack length, with microscale damaged fiber bundle bridging ligaments, in support of the CZM approach and the softening relation presented in Appendix C (Eq. (8)-(9)).

Properties of the calibrated CZM_{LT} (adjusted to fit global specimen behavior) are given in Table 2; the values of the parameters φ_n^{LT}, σ_{ccs}^{LT} and α are adjusted by minimizing the discrepancy between FEM predictions and experimental load–displacement data, see Fig. 6b. Details of how the values on φ_n^{LT}, σ_{ccs}^{LT}, and α are optimized are found in Appendix C. For analysis of the CZM_{LT} parameters, Fig. 6b-d are helpful. By first comparing Table 1 and Table 2, φ_n^{LT} for Birch/PMMA and D-Birch/PMMA are larger than the J_c values and as high as ≈ 16 kJ/m^2. The cohesive strength, σ_{ccs}^{LT}, in Table 2 for D-Birch/PMMA and Birch has decreased compared to Table 1. This means that σ_{ccs}^{LT} is lower than the nominal tensile strength of the material measured from previous tensile tests. The introduction of a polymer matrix in wood cell lumen for Birch/PMMA and D-Birch/PMMA is apparent on σ_{ccs}^{LT}, which is doubled compared to neat Birch. The adjusted shape of the CZM_{LT} is also of interest, as expressed by the shape parameter α. For D-Birch/PMMA, the calibrated softening shape is concave, which means that a sudden load drop occurs only close to δ_{cn}^{LT} and not at the peak load, as for $\alpha > 2.0$, which has a convex softening shape (see Fig. 2b). The scale of δ_{cn}^{LT} in the CZM_{LT} (see Table 2) is interesting since the values can be as high as ≈ 0.12 mm, so the critical separation for LT cracks is at a large scale in these materials compared to materials such as metals and ceramics. One consequence is that the present biocomposites are much less sensitive to preexisting defects, e.g., from processing. In Fig. 6c, the fracture process zone development of D-Birch/PMMA is interpreted using the CZM in Fig. 6d with CZM_{LT} parameters from Table 2. Early in the load–displacement curve in Fig. 6c, the non-linear behavior and damage development are initiated when $\sigma_n = \sigma_{ccs}^{LT}$, and crack growth occurs after F_{max} when

Table 2
Calibrated CZM_{LT} parameters: (φ_n^{LT}, σ_{ccs}^{LT}, and δ_n^{LT}) determined by minimized load–displacement differences between experiment and FEM by updating. δ_{cn}^{LT} is incorporated into the PPR model and determined by Equation (9). The results presented are from a single specimen of each material.

	LT fracture plane				Characteristic material length [17]
Material	φ_n^{LT}[kJ/m^2]	σ_{ccs}^{LT}[MPa]	α	δ_{cn}^{LT}[μm]	$\delta_{cn}^{LT}E_L/\sigma_{ccs}^{LT}$[mm]
(Birch**)	(16**)	(111)	(1.5)	(216)	(32)
Birch (Table 1)	8*	175*	2.0*	92*	9
Birch/PMMA	16	260	1.7	105	6
D-Birch/PMMA	16	220	1.7	124	11

* Rounded values are imported from Table 1, and an assumed linear cohesive softening behavior with $\alpha = 2$.
** This value for neat Birch overestimates the "true" φ_n^{LT}, since specimen effects from compression failure and creep are included.

$\delta_n = \delta_{cn}^{LT}$ and $\sigma_n = 0$. Overall, the CZM data in Table 2 provide more detailed information on fracture properties than the point-based values for J_c, and CZM parameters depend on microstructural details (e.g., volume fraction of wood reinforcement).

For neat Birch, the calibration results in much larger φ_n^{LT} values than previous estimates for J_c; see Table 1 and Fig. 3d. There is a large discrepancy between FEM and experiments in the load–displacement curves for Birch, but not for Birch/PMMA and D-Birch/PMMA. The initial experimental response for Birch is more compliant than FEM predictions. Possibly, there is large non-linear deformation at other locations than in the crack tip damage region. This is in the form of creep or compression failure in the region where steel rollers are in contact with the upper part of the specimen, as noted in previous 4 PB fracture tests [18]. Compression failure was previously in observed native 4 PB wood specimens and addressed by filling wood porosity with PMMA [33]. From the FE-model of Birch, large compressive stresses are observed in the fiber direction on the upper side of the specimen and much higher than compressive strength (lower than tensile strength for porous wood). However, compressive failure energy (and possibly creep effects) are included in the φ_n^{LT} for Birch, so that φ_n^{LT} is overestimated. For Birch, φ_n^{LT}= 8 kJ/m^2, from J_c in Table 1, is probably closer to the real fracture energy.

The side-grooves promote crack growth in the LT fracture plane. Micrographs in Figs. 4-5 showed that 90° crack deflection along the TL fracture plane was also present in the side-grooved specimens, with multiple microcracks parallel to the load axis at about every 200 μm, shown in Fig. 4a. Short TL fracture planes with TL CZM parameters (CZM_{TL}) were therefore included in the FE-model (Fig. 2a). Here, CZM_{TL} parameters from previous TL fracture tests are used [18]. The effects of such microcracks on specimen load–displacement curves are modeled, showing negligible influence; see Fig. A5b. In the FE-model, which includes CZM_{LT} and CZM_{TL} (Fig. A5a), the TL crack paths are short, but even if the length of the cohesive zones were extended beyond the side-grooves, there were negligible effects on the load–displacement curves.

In the context of fiber bridging mechanisms, a characteristic material length, m, (inspired by Bao and Suo [17]) can be estimated by,

$$m = \frac{\delta_{cn} E}{\sigma_{ccs}}, \tag{4}$$

where E is Young's modulus of the solid [17], here E is assumed to be Young's modulus in the loading direction, E_L. The parameter m is related to the length of a fully developed DZ, L_0, which is reached when the strain energy release rate is equal to the fracture energy of the material, where larger forces are not needed to maintain a steady crack growth. In Eq. (4), m is calculated based on the CZM_{LT} for all materials from Table 2. Data show that the scale of the DZ for LT crack growth can be larger than 10 mm. For Birch, J_c from experiments results in a slightly larger material length than Birch/PMMA and shorter than D-Birch/PMMA mainly due to different α and σ_{ccs}^{LT}. To relate m to specimen dimension, a ratio between initial crack length a_0 and m gives values ≈ 0.1, which means that the characteristic material length is larger than the initial crack length (large-scale bridging). DZ lengths from TL fracture mechanics tests have been measured to about 100 mm at stable crack growth for other wood and wood-polymer composites using specimen geometries with a $a_0/m > 1.0$ [34]. A fully developed DZ cannot be obtained with the present specimen dimensions. Although the present CZM_{LT} parameters are theoretically applicable to large-scale bridging cases, they need to be verified for other specimen dimensions and load cases.

5. Conclusions

For the first time, the high toughness of wood composites, where wood pore space is filled with a thermoplastic polymer, was analyzed by non-linear fracture mechanics suitable for composites. The problem of 90° crack deflection was successfully avoided by side-grooved 4 PB single-edge pre-cracked specimens to promote cross-grain LT crack growth. The main toughening mechanisms in the damage zone (DZ) were fiber bundle bridging and pull-out. It was observed that the scale of limiting separation, δ_n^{LT}, at the end of the DZ was $\approx$ 100 μm, and that the physics of the DZ was suitable for cohesive zone modeling (CZM).

The fracture properties, cohesive zone strength, σ_{ccs}^{LT}, limiting separation, δ_n^{LT}, and fracture energy, φ_n^{LT}, were estimated with a softening CZM. Finite element analysis using orthotropic linear elasticity was combined with a CZM to model the DZ and compared with load–displacement data from the fracture mechanics experiment. Based on experiments, an initial "guess" for the CZM parameters was optimized so that the composite specimens showed a good fit to experimental data. Compared with neat birch, the polymer-filled composites showed much higher fracture energy φ_n^{LT} (16 kJ/m^2 vs 8 kJ/m^2). The main reason is increased σ_{ccs}^{LT} in the DZ. The polymer matrix contributes load-bearing capacity but the microscale stress distribution in the wood fiber cell wall is probably also more homogeneous so that local σ_{ccs}^{LT} is increased.

The cohesive zone modeling approach extends the dominating linear elastic fracture mechanics approach for wood fracture toughness and includes wood-polymer composites. Fracture and crack growth under conditions of large-scale damage behind the crack tip can therefore be predicted for the materials. Perhaps the most significant step forward is that the CZM parameters are a tool to improve wood biocomposites toughness by controlling microstructure. By systematic variation of constituents, reinforcement volume fraction, wood-polymer interface properties we should be able to tailor CZM fracture properties. For validation of the approach in the context of engineering design, other specimen geometries and a larger number of specimens need to be investigated.

Data availability

Data will be made available on request.

Declaration of Competing Interest

The authors declare that they have no known competing financial interests or personal relationships that could have appeared to influence the work reported in this paper.

Acknowledgments

Dr. M. Höglund and Dr. C. Montanari for helping to produce transparent wood biocomposites. Dr. A. Riazanova and Treesearch Research Infrastructure for support with FE-SEM imaging and installation of the DEBEN microstage in the FE-SEM. We acknowledge funding from European Research Council (ERC) under the European Union's Horizon 2020 research and innovation program (grant agreement No. 742733). We also acknowledge financial support from Knut and Alice Wallenberg (KAW) foundation through the Wallenberg Wood Science Center.

Appendix A

A. In situ 4PB fracture testing

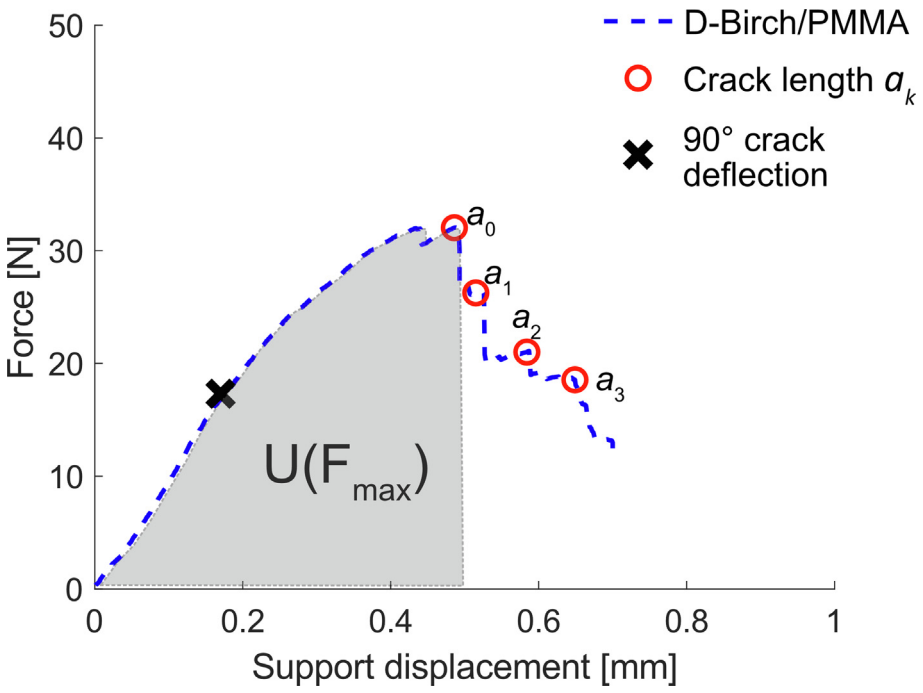

Fig. A1. Sketch of how $U(F_{max})$ was evaluated using the load–displacement curve of the D-Birch/PMMA specimen shown in Fig. 3c.

B. Additional images of micromechanisms of crack growth

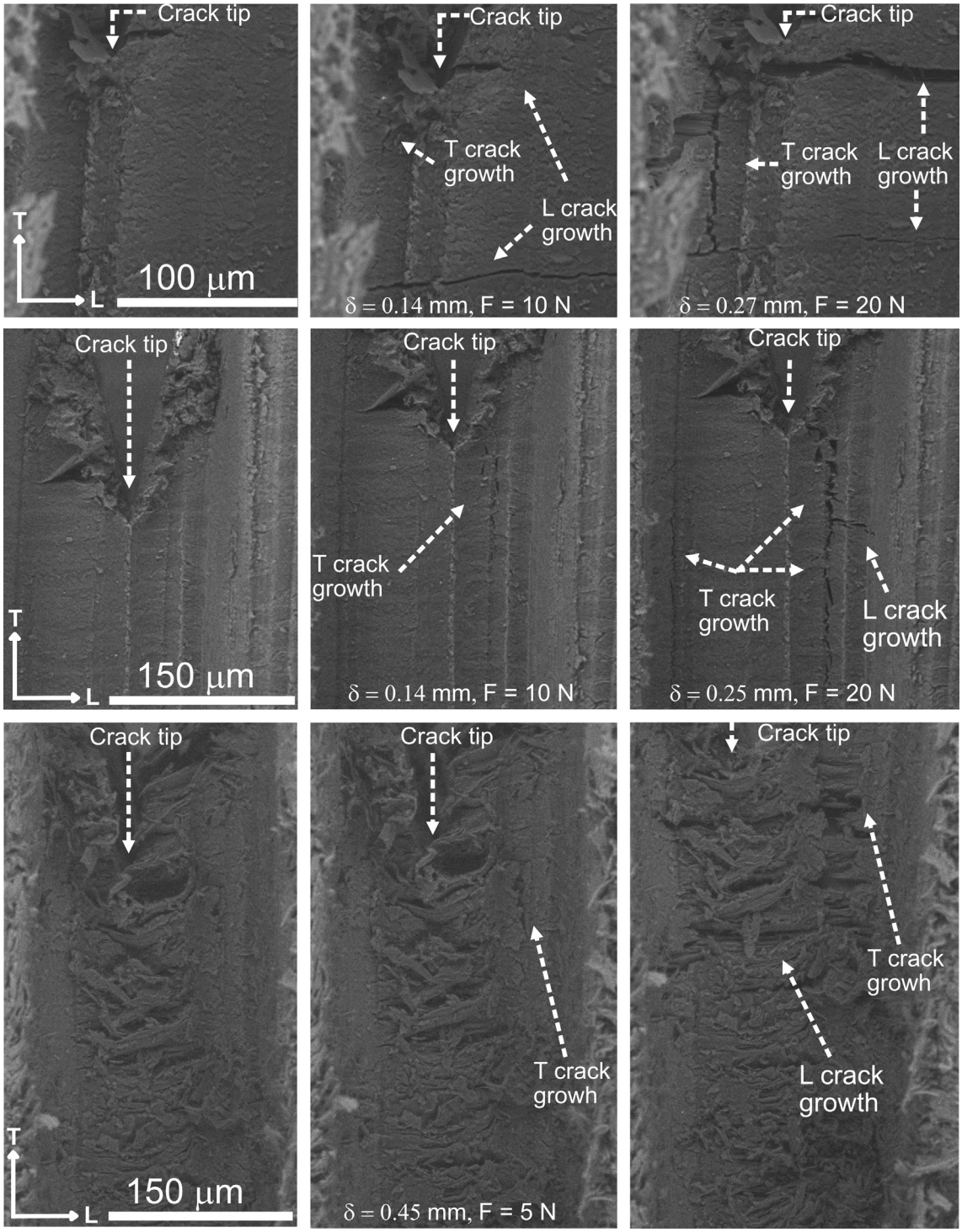

Fig. A2. Fractography images of D-Birch/PMMA (Upper), Birch/PMMA (Middle), and native birch (lower), with sequential images taken during crack propagation. Images show crack propagation along T and L directions at different sequences. Displacement of the machine supports δ_{piston} and measured force F are noted in the images.

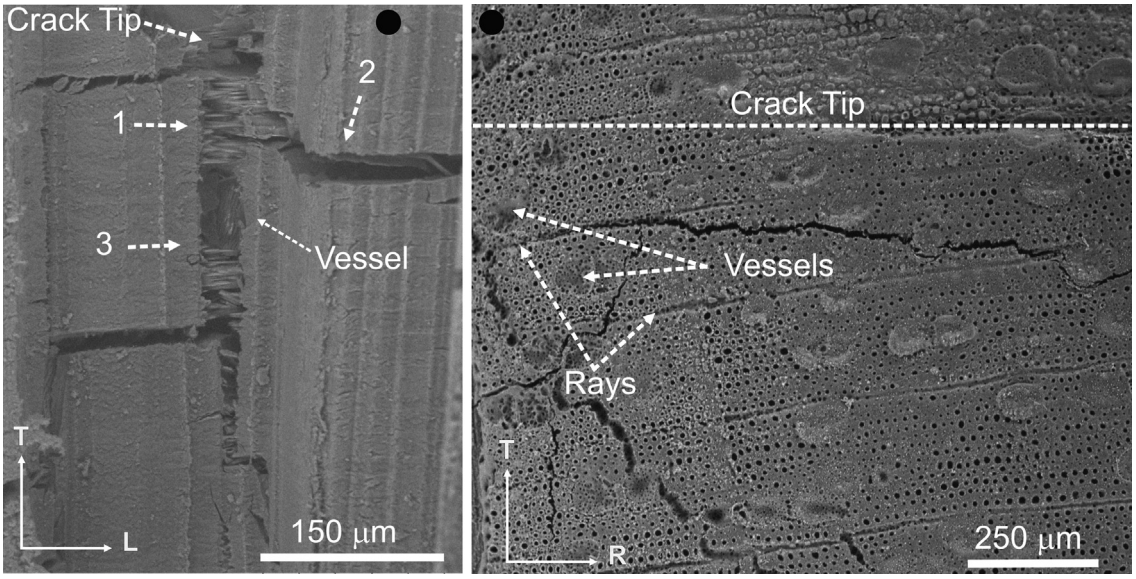

Fig. A3. Fractography of Birch/PMMA with numbered sequences (e.g., 1, 2 and 3) indicating the order of fracture event observed by the in situ 4 PB test in SEM. Subsequent images can see in Fig. A2. The left image shows initial crack growth along the T-direction and subsequential crack propagation along T and L-direction. The right image is a straight laser-cut cross-section along the fourth growing crack path seen in the left image. The red dot in the upper left corner of the right image indicates the surface observed in SEM on the left image. (For interpretation of the references to colour in this figure legend, the reader is referred to the web version of this article.)

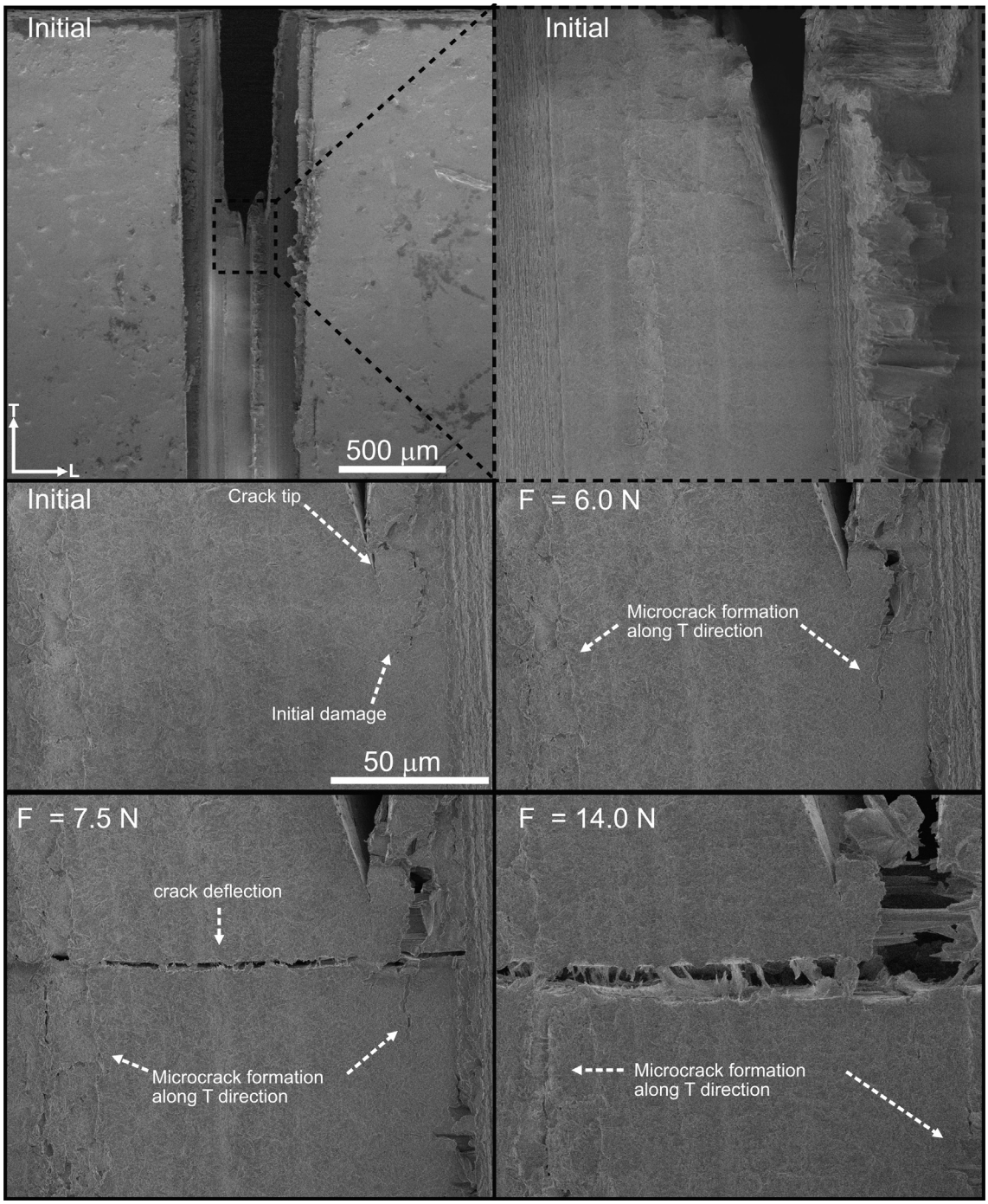

Fig. A4. Sequential in-situ FE-SEM images of D-Birch/PMMA side-grooved sample. Upper row images are overview of the sample with no load. The middle row left image shows the initial state around the crack tip, and the right image shows a sample with applied load. The lower row shows images with sudden 90° crack deflection and LT microcrack formation below.

C. FE-model with cohesive fracture zone

The cohesive zone model, PPR, is formulated for mixed-mode fracture but can also be used to evaluate for mode I fracture. The 4 PB bending load case is symmetric, and a mode I fracture is reasonable if the crack propagates along the LT fracture plane. In Figs. 4-5, microcracks by 90° crack deflection are apparent, which may exhibit mixed-mode fracture. Therefore, useful to implement the PPR for mixed-mode fracture in the FE model presented in Fig. 6c.

The cohesive zone deformation is split into an opening (normal to fracture surface), δ_n, and in-plane tangential (parallel to fracture surface), δ_t, displacements. The opening stress, σ_n, and in-plane shear stress, τ, are defined as

$$\begin{aligned}\sigma_n(\delta_n,\delta_t) &= -\alpha\Gamma_n\frac{1}{\delta_{cn}}\left(1-\frac{\delta_n}{\delta_{cn}}\right)^{\alpha-1}\left[\Gamma_t\left(1-\frac{|\delta_t|}{\delta_{ct}}\right)^{\beta}+\langle\varphi_t-\varphi_n\rangle\right],\\ \tau(\delta_n,\delta_t) &= -\beta\Gamma_t\frac{1}{\delta_{ct}}\left(1-\frac{|\delta_t|}{\delta_{ct}}\right)^{\beta-1}\left[\Gamma_n\left(1-\frac{\delta_n}{\delta_{cn}}\right)^{\alpha}+\langle\varphi_n-\varphi_t\rangle\right]\frac{\delta_t}{|\delta_t|}\end{aligned} \quad (5)$$

where α and β are shape parameters for the opening and shear stresses, respectively; the corresponding fracture energies φ_n and φ_t are given by $\Gamma_n = (-\varphi_n)^{\frac{\langle\varphi_n-\varphi_t\rangle}{(\varphi_n-\varphi_t)}}$, and $\Gamma_t = (-\varphi_t)^{\frac{\langle\varphi_t-\varphi_n\rangle}{(\varphi_t-\varphi_n)}}$ (if $\varphi_n = \varphi_t$, then $\Gamma_n = -\varphi_n$ and $\Gamma_t = 1$). Finally, δ_{cn} and δ_{ct} are the critical opening displacements [27]. The softening damage behavior initiates when $\sigma_n = \sigma_{ccs}$ or $\tau = \tau_{ccs}$, and complete separation of the fracture surfaces occurs when $\sigma_n(\delta_{cn}, \delta_t) = 0$, or $\tau(\delta_n, \delta_{ct}) = 0$. Here, the critical opening displacements are defined as,

$$\begin{aligned} \delta_{cn} &= \alpha\varphi_n/\sigma_{ccs}, \\ \delta_{ct} &= \beta\varphi_t/\tau_{ccs}. \end{aligned} \tag{6}$$

The initial linear contribution from the cohesive zone to the specimen deformation was assumed negligible; hence, the cohesive zone only exhibits softening damage behavior. The advantage of the PPR cohesive model is that the softening relation is easily changed by the two functional shape parameters α and β. The value $\alpha = \beta = 2$ results in almost linear softening behavior. Larger values than 2 result in a convex functional shape, similar to more brittle fracture behavior, and lower values than 2 in a concave shape.

Load-displacement curve discrepancy between FE-model and experimental is minimized by calibrating the values on φ_n, σ_{ccs}, and α. This is done using a Nelder-Mead optimization algorithm with the objective function

$$\min\ \Omega = \| F_{exp} - F_{FEM}(\varphi_n, \sigma_{ccs}, \alpha) \| \tag{7}$$

where F_{exp} is the force measured experimentally from the load cell, F_{FEM} is the force from FE-model which also depends on CZM parameters φ_n, σ_{ccs}, and α. The load points to minimize using Eq. (7) was chosen based on same support displacement δ_{piston}.

A mesh convergence of the FE-model is shown in Fig. A7.

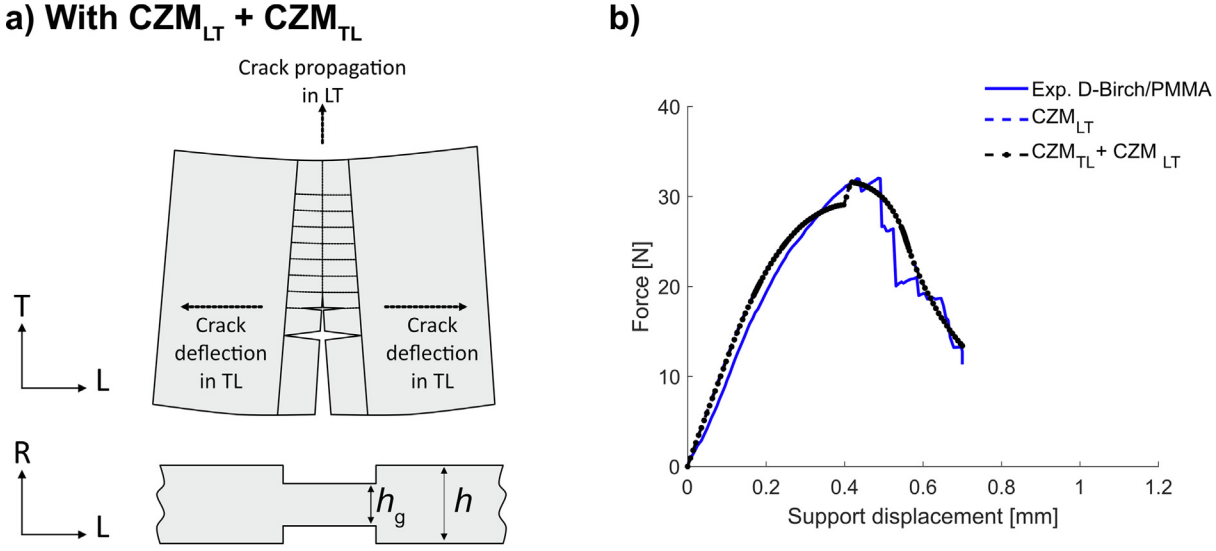

Fig. A5. Side-grooved specimen model in FEM with one CZM_{LT} and several cohesive zones in TL-direction placed according to the sketch, with 200 μm distance between each TL cohesive zone along the L-direction. CZM_{LT} parameters are from Table 2, and CZM_{TL} from previous fracture tests [18]. d) Experimental and FEM load–displacement data with the two different proposed models, see Fig. 2a and Fig. A5a.

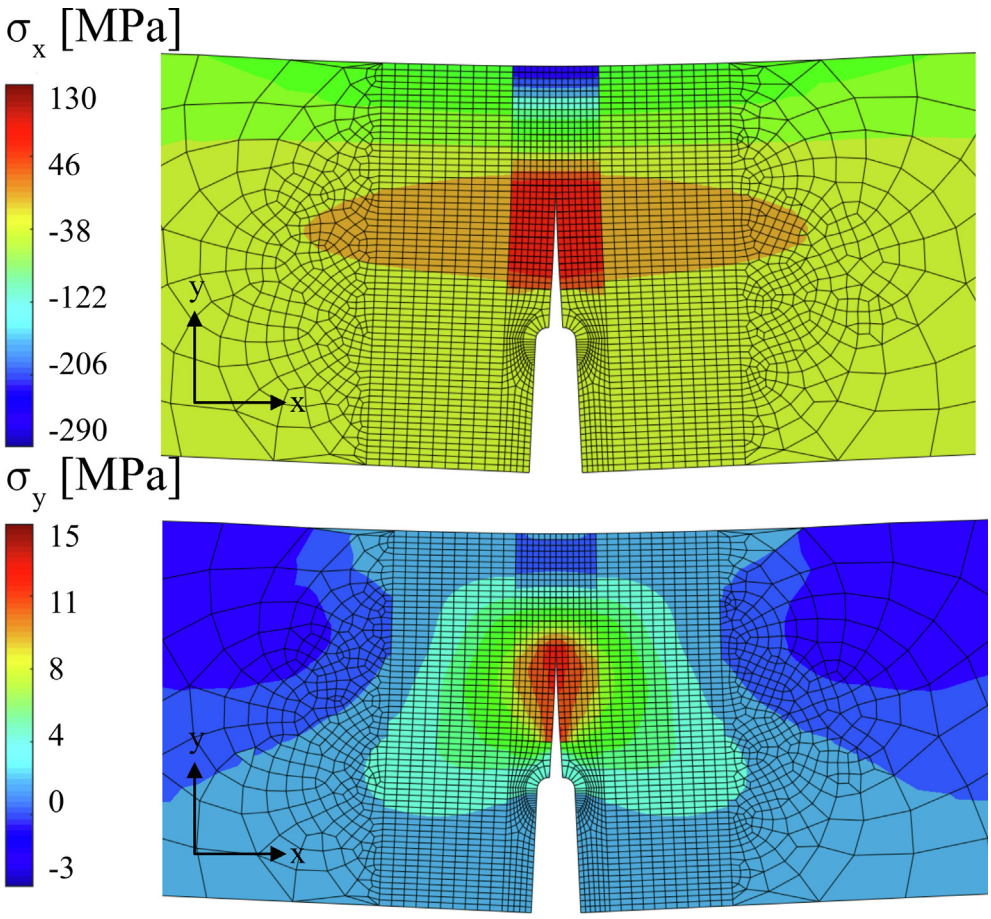

Fig. A6. FEM results of native birch with typical stress distribution at peak load (≈30 N) of a side-groove specimen along x and y directions (noted in the images). Material direction L is along the x-direction and material direction T is along the y-direction. Cohesive zones are placed in the LT and TL fracture planes, according to Fig. 6a.

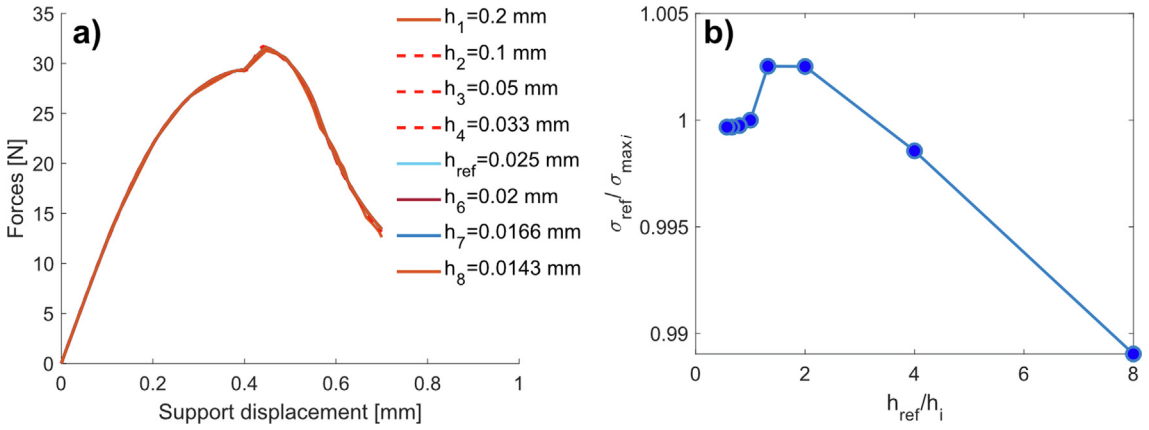

Fig. A7. Mesh refinement with element size measured at the cohesive zone where h_i is the different mesh sizes and h_{ref} = 0.025 mm. a) Load-displacement data from FEM with different element sizes. b) Relative maximal stress to the reference maximal stress from h_{ref} = 0.025 mm.

Appendix B. Supplementary data

Supplementary data to this article can be found online at https://doi.org/10.1016/j.matdes.2023.112058.

References

[1] Y. Li, Q. Fu, S. Yu, M. Yan, L. Berglund, Optically transparent wood from a nanoporous cellulosic template: combining functional and structural performance, Biomacromolecules 17 (2016) 1358–1364, https://doi.org/10.1021/acs.biomac.6b00145.
[2] C. Montanari, P. Olsén, L.A. Berglund, Sustainable wood nanotechnologies for wood composites processed by in-situ polymerization, Front. Chem. 9 (2021) 483, https://doi.org/10.3389/fchem.2021.682883.
[3] Y. Li, S. Yu, J.G.C. Veinot, J. Linnros, L. Berglund, I. Sychugov, Luminescent transparent wood, Adv. Opt. Mater. 5 (2017) 3–7, https://doi.org/10.1002/adom.201600834.
[4] C. Montanari, Y. Ogawa, P. Olsén, L.A. Berglund, High performance, fully bio-based, and optically transparent wood biocomposites, Adv. Sci. 8 (2021) 2100559, https://doi.org/10.1002/advs.202100559.

[5] C. Montanari, Y. Li, H. Chen, M. Yan, L.A. Berglund, Transparent wood for thermal energy storage and reversible optical transmittance, ACS Appl. Mater. Interfaces 11 (2019) 20465–20472, https://doi.org/10.1021/acsami.9b05525.
[6] Y. Li, Q. Fu, X. Yang, L. Berglund, Transparent wood for functional and structural applications, Philos Trans R Soc, A 376 (2112) (2018) 20170182.
[7] L.J. Gibson, M.F. Ashby, Wood, in: L.J. Gibson, M.F. Ashby (Eds.), Cellular Solids Structure and Properties, second ed., Cambridge University Press, Cambridge, 1997, pp. 387–428.
[8] H.L. Bernstein, Fracture toughness of polycarbonate as characterized by the J-integral, ASTM Spec. Tech. Publ. (1991) 306–319.
[9] G. Jeronimidis, The fracture behaviour of wood and the relations between toughness and morphology, Proc. R. Soc. London Ser. B, Biol. Sci. 208 (1980) 447–460.
[10] G. Jeronimidis, The fracture of wood in relation to its structure, Leiden Bot. Ser. 3 (1976) 253–265, https://doi.org/10.1145/2212757.2212763.
[11] J.E. Gordon, G. Jeronimidis, Work of fracture of natural cellulose, Nature 252 (5479) (1974) 116.
[12] M.F. Ashby, K.E. Easterling, R. Harrysson, S.K. Maiti, The Fracture and toughness of woods, Proc. R. Soc. A Math. Phys. Sci. 398 (1985) 261–280.
[13] A.P. Schniewind, Fracture toughness and duration of load factor II. duration factor for cracks propagating perpendicular-to-grain, Wood Fiber Sci. 9 (1977) 216–226.
[14] H.G. Tattersall, G. Tappin, The work of fracture and its measurement in metals, ceramics and other materials, J. Mater. Sci. 1 (1966) 296–301, https://doi.org/10.1007/BF00550177.
[15] M.J. Chappell, J.G. Morley, The fracture toughness of conventional materials and composite systems containing non-fracturing reinforcing elements, J. Mater. Sci. 11 (1976) 57–70, https://doi.org/10.1007/BF00541075.
[16] M.H. Schneider, S. Vasic, S. Lande, J.G. Phillips, Static bending and toughness of wood polymer composites (yellow birch and basswood), Wood Sci. Technol. 37 (2003) 165–176, https://doi.org/10.1007/s00226-003-0189-1.
[17] G. Bao, Z. Suo, Remarks on crack-bridging concepts, Appl. Mech. Rev. 45 (1992) 355–366.
[18] E. Jungstedt, S. Östlund, L.A. Berglund, Transverse fracture toughness of transparent wood biocomposites by FEM updating with cohesive zone fracture modeling, Compos. Sci. Technol. 225 (2022) 1–10, https://doi.org/10.1016/j.compscitech.2022.109492.
[19] D. Supriatna, B. Yin, D. Konopka, M. Kaliske, An anisotropic phase-field approach accounting for mixed fracture modes in wood structures within the Representative Crack Element framework, Eng. Fract. Mech. 269 (2022), https://doi.org/10.1016/j.engfracmech.2022.108514 108514.
[20] S. Pech, M. Lukacevic, J. Füssl, A hybrid multi-phase field model to describe cohesive failure in orthotropic materials, assessed by modeling failure mechanisms in wood, Eng. Fract. Mech. 271 (2022), https://doi.org/10.1016/j.engfracmech.2022.108591 108591.
[21] E. Jungstedt, C. Montanari, S. Östlund, L. Berglund, Mechanical properties of transparent high strength biocomposites from delignified wood veneer, Compos. A 133 (2020), https://doi.org/10.1016/j.compositesa.2020.105853 105853.
[22] A.P. Schniewind, J.C. Centeno, Fracture toughness and duration of load factor I. six principal systems of crack propagation and the duration factor for cracks propagating parallel to grain, Wood Fiber Sci. 5 (1973) 152–159.
[23] Y. Li, Q. Fu, X. Yang, L. Berglund, Transparent wood for functional and structural applications, Philos. Trans. R. Soc., A 376 (2018) 20170182, https://doi.org/10.1098/rsta.2017.0182.
[24] B.F. Sørensen, P. Brethe, P. Skov-Hansen, Controlled crack growth in ceramics: The DCB specimen loaded with pure moments, J. Eur. Ceram. Soc. 16 (1996) 1021–1025, https://doi.org/10.1016/0955-2219(96)00021-0.
[25] J.E. Lindhagen, L.A. Berglund, Application of bridging-law concepts to short-fibre composites Part 1: DCB test procedures for bridging law and fracture energy, Compos. Sci. Technol. 60 (6) (2000) 871–883.
[26] J.R. Rice, P.C. Paris, J.G. Merkle, Some further results of J-integral analysis and estimates, ASTM Spec. Tech. Publ. (1972) 231–245, https://doi.org/10.1520/stp49643s.
[27] K. Park, G.H. Paulino, J.R. Roesler, A unified potential-based cohesive model of mixed-mode fracture, J. Mech. Phys. Solids 57 (2009) 891–908, https://doi.org/10.1016/j.jmps.2008.10.003.
[28] K. Park, G.H. Paulino, Computational implementation of the PPR potential-based cohesive model in ABAQUS: Educational perspective, Eng. Fract. Mech. 93 (2012) 239–262, https://doi.org/10.1016/j.engfracmech.2012.02.007.
[29] Q. Chen, Z. Jiang, X. Pei, Y. Liu, R. Du, G. Zhao, Bio-inspired, epoxy-based lamellar composites with superior fracture toughness by delignified wood scaffold, Compos. Sci. Technol. 207 (2021), https://doi.org/10.1016/j.compscitech.2021.108739 108739.
[30] M.H. Schneider, J.G. Phillips, K.I. Brebner, D.A. Tingley, Toughness of polymer impregnated sugar maple at two moisture contents, For. Prod. J. 39 (1989) 11–14.
[31] R.K. Bordia, B.J. Daigleish, P.G. Charalambides, A.G. Evans, Cracking and damage in a notched unidirectional fiber-reinforced brittle matrix composite, J. Am. Ceram. Soc. 74 (1991) 2776–2780, https://doi.org/10.1111/j.1151-2916.1991.tb06842.x.
[32] A. Kelly, Interface effects and the work of fracture of a vibrous composite, Proc. R. Soc. London A Mater. Phys. Sci. 319 (1970) 95–116, https://doi.org/10.1098/rspa.1970.0168.
[33] G. Scurfield, S.R. Silva, M.B. Wold, Failure of wood under load applied parallel to grain: A study using scanning electron microscopy, Micron 1971 (3) (1969) 160–184, https://doi.org/10.1016/0047-7206(71)90054-9.
[34] B. Mirzaei, A. Sinha, J.A. Nairn, Using crack propagation fracture toughness to characterize the durability of wood and wood composites, Mater. Des. 87 (2015) 586–592, https://doi.org/10.1016/j.matdes.2015.08.010.